Supplementary Information

Transition-Metal-Doped WSe_2 Homojunctions for Multifunctional Logic and Optoelectronic Devices

Vu Khac Dat[1†], Minh Chien Nguyen[2†], Hai Phuong Duong[3†], Tien Dat Ngo[4†], Mallesh Baithi[2], Van Dam Do[2], Chengyun Hong[5], Van Cao Nguyen[3], Thi Uyen Tran[6], Dinh Hoa Luong[3], Ki Kang Kim[3], Seong Chu Lim[2], Quynh Le-Van[1], Woo Jong Yu[2*], Tuan Dung Nguyen[1*] and Ngoc Thanh Duong[7*]

Affiliations

[1]Center for Materials Innovation and Technology (CMIT), College of Engineering and Computer Science, VinUniversity, Gia Lam District, Hanoi 10000, Vietnam

[2]Department of Electrical and Computer Engineering, Sungkyunkwan University, Suwon 16419, Republic of Korea.

[3]Department of Energy Science, Sungkyunkwan University, Suwon 16419, Republic of Korea.

[4]Imec, Remisebosweg 1, B-3001 Leuven, Belgium

[5]Department of Materials Science and Engineering, Pohang University of Science and Technology, Pohang, Republic of Korea

[6]SKKU Advanced Institute of Nano Technology, Sungkyunkwan University, Suwon 16419, Republic of Korea

[7]Faculty of Materials Science and Engineering, Phenikaa School of Engineering, Phenikaa University, Hanoi 12116, Vietnam

[†]These authors contributed equally to this work.

*Corresponding emails: thanh.duongngoc1@phenikaa-uni.edu.vn, dung.nt9@vinuni.edu.vn, micco21@skku.edu,

Contents

Supplementary Figure 18. AFM characterization of a thick V-doped/pristine WSe_2 heterostructure.

Supplementary Figure 19. Thickness-dependent gate modulation in pristine and V-doped WSe_2.

Supplementary Figure 20. Gate-controlled photocurrent polarity switching

Supplementary Figure 21. Power-dependent photoresponse under 458 nm illumination.

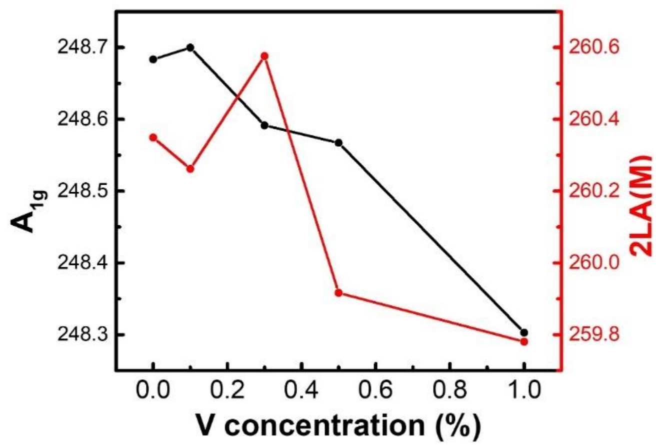

Supplementary Figure 1. **Vanadium doping concentration–dependent Raman phonon modes of V-doped WSe_2.** Evolution of the A_{1g} and 2LA(M) phonon frequencies as a function of V doping concentration, reflecting systematic lattice modification induced by substitutional V incorporation at W sites. The absence of additional Raman modes indicates that the WSe_2 crystal structure is preserved without the formation of secondary phases.

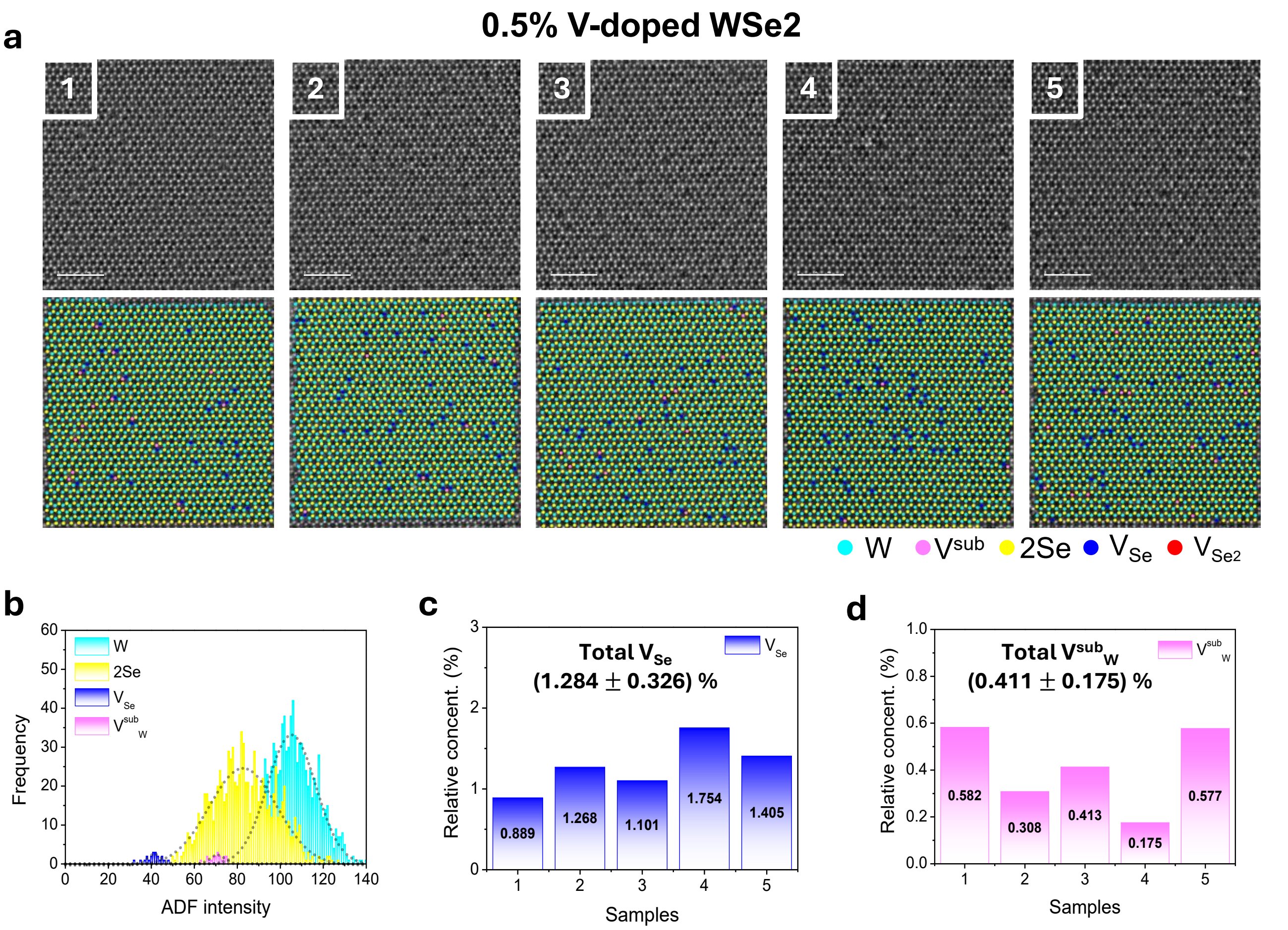

Supplementary Figure 2. Atomic-scale analysis of substitutional V doping in 0.5% V-doped WSe_2 by ADF-STEM. (a) Atomic-resolution annular dark-field scanning transmission electron microscopy (ADF-STEM) images acquired from five different positions (1-5) of a 0.5% V-doped WSe_2 sample, together with the corresponding atomically resolved, false-color–mapped images. The color mapping identifies W atoms (cyan), Se atoms (yellow), V atoms substituted into W sites (V^{sub}_W, pink), and Se vacancies (V_{Se}, red). Scale bar 2nm. **(b)** Normalized ADF intensity histograms of the different atomic columns extracted from the images in **(a)**, showing distinct intensity distributions that enable reliable identification of W, Se, and V-related atomic sites. **(c)** Vacancy density (V_{Se} %) extracted from the five sampled regions, yielding an average total V_{Se} concentration of (1.284 ± 0.326)%. **(d)** Relative concentration of substitutional vanadium at tungsten sites (V^{sub}_W) for the same regions, with an average concentration of (0.411 ± 0.175)% .

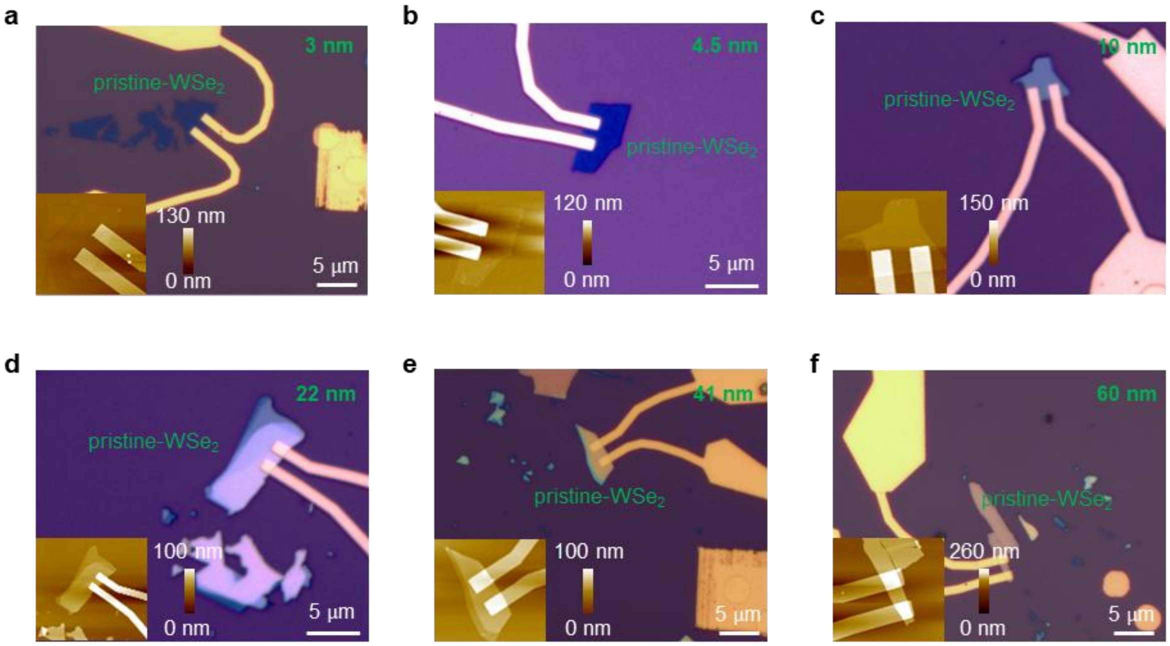

Supplementary Figure 3. Thickness characterization of pristine WSe_2 FET devices. (a–f) Optical microscopy images of pristine WSe_2 flakes used for device fabrication, with insets showing corresponding AFM height profiles. The extracted thicknesses are approximately 3, 4.5, 10, 22, 41, and 60 nm, respectively.

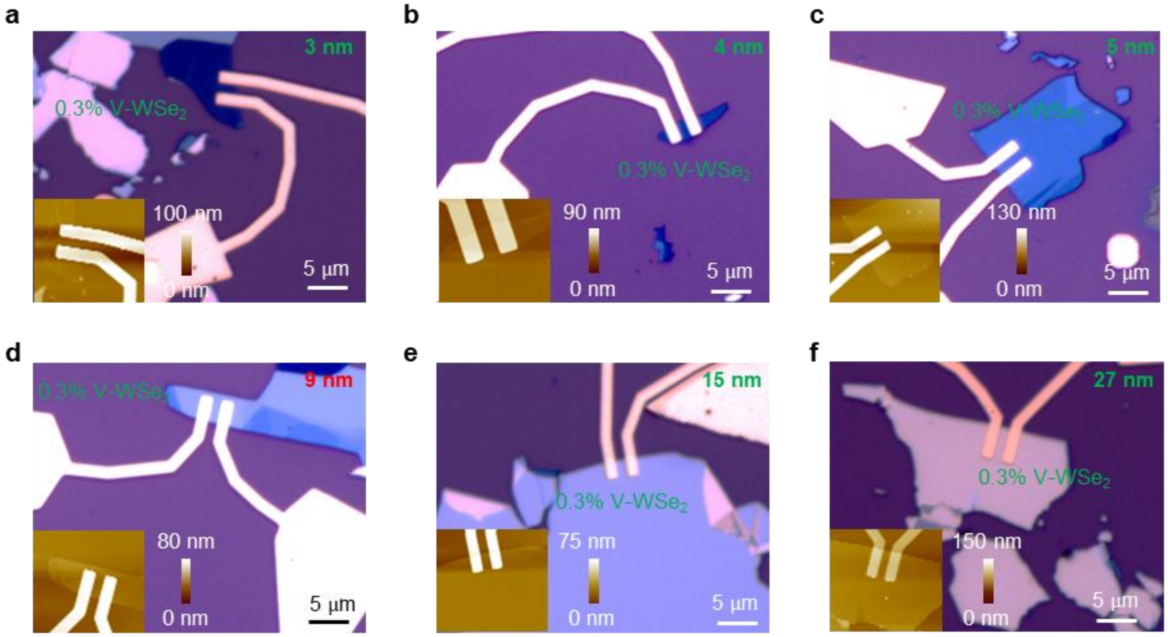

Supplementary Figure 4. Thickness characterization of 0.3% V-doped WSe_2 FET devices. (a–f) Optical microscopy images of 0.3% V-doped WSe_2 flakes with corresponding AFM height profiles, indicating thicknesses of approximately 3, 4, 5, 9, 15, and 27 nm.

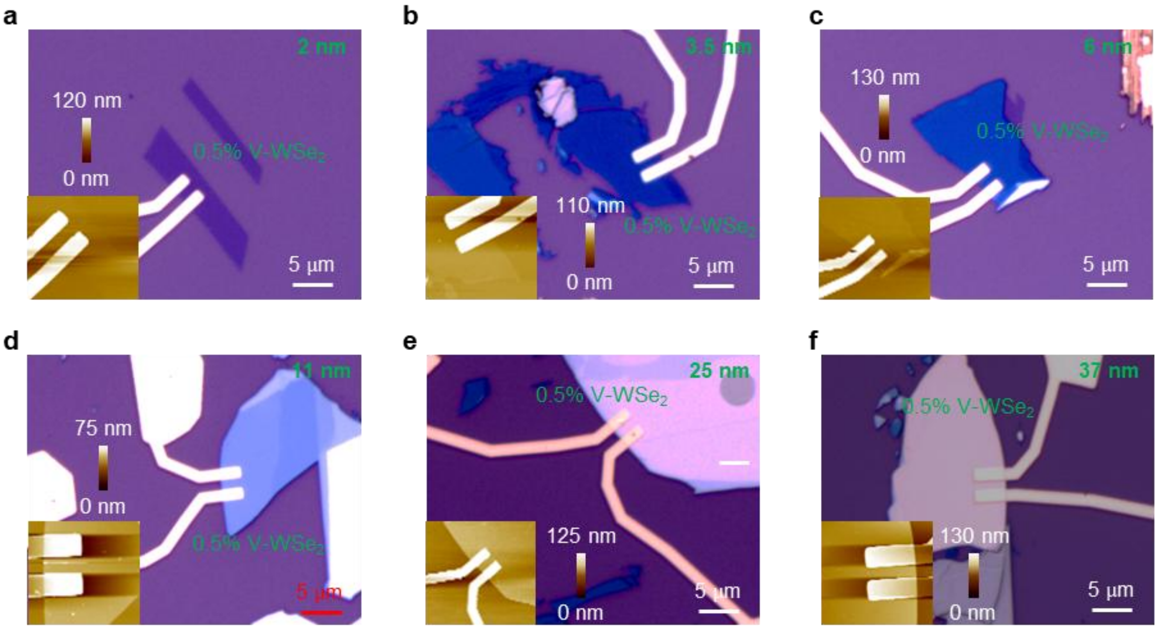

Supplementary Figure 5. Thickness characterization of 0.5% V-doped WSe_2 FET devices. (a–f) Optical microscopy images and AFM height profiles of 0.5% V-doped WSe_2 flakes with thicknesses of approximately 2, 3.5, 6, 11, 25, and 37 nm.

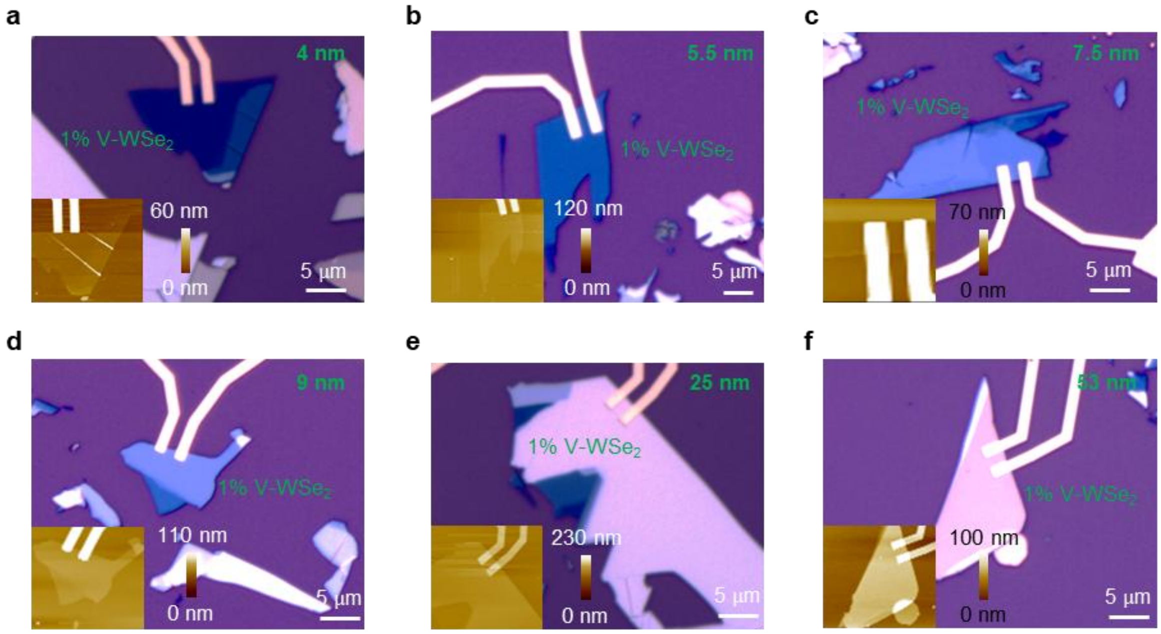

Supplementary Figure 6. Thickness characterization of 1% V-doped WSe_2 FET devices. (a–f) Optical microscopy images and corresponding AFM height profiles of 1% V-doped WSe_2 flakes with thicknesses of approximately 4, 5.5, 7.5, 9, 25, and 53 nm.

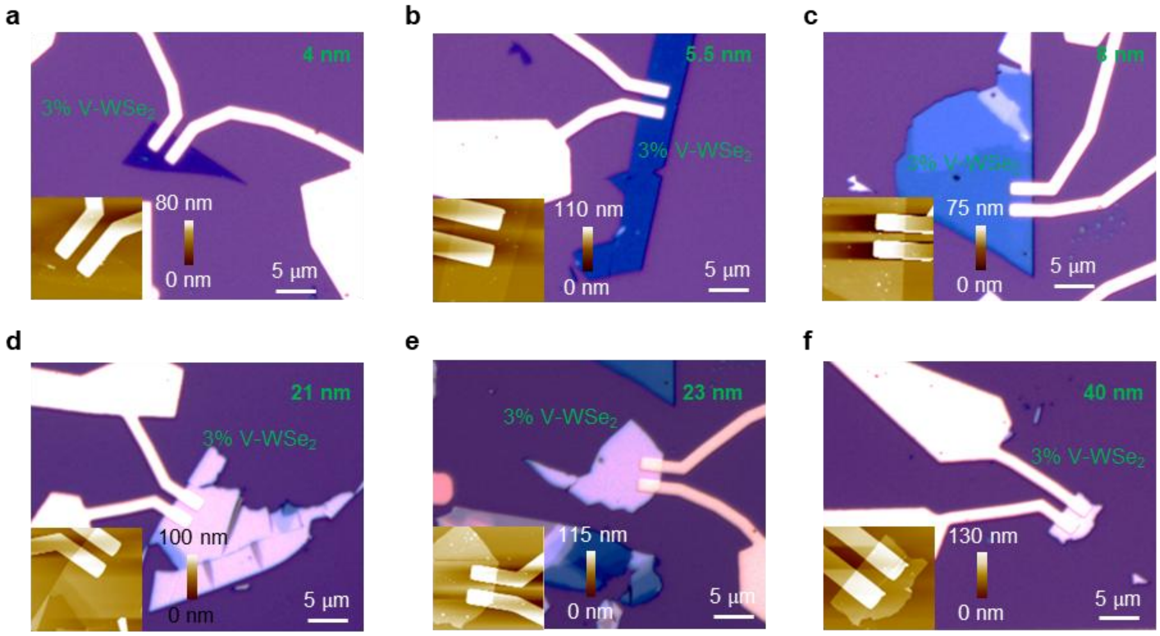

Supplementary Figure 7. Thickness characterization of 3% V-doped WSe_2 FET devices. (a–f) Optical microscopy images and AFM height profiles of 3% V-doped WSe_2 flakes with thicknesses of approximately 4, 5.5, 8, 21, 23, and 40 nm.

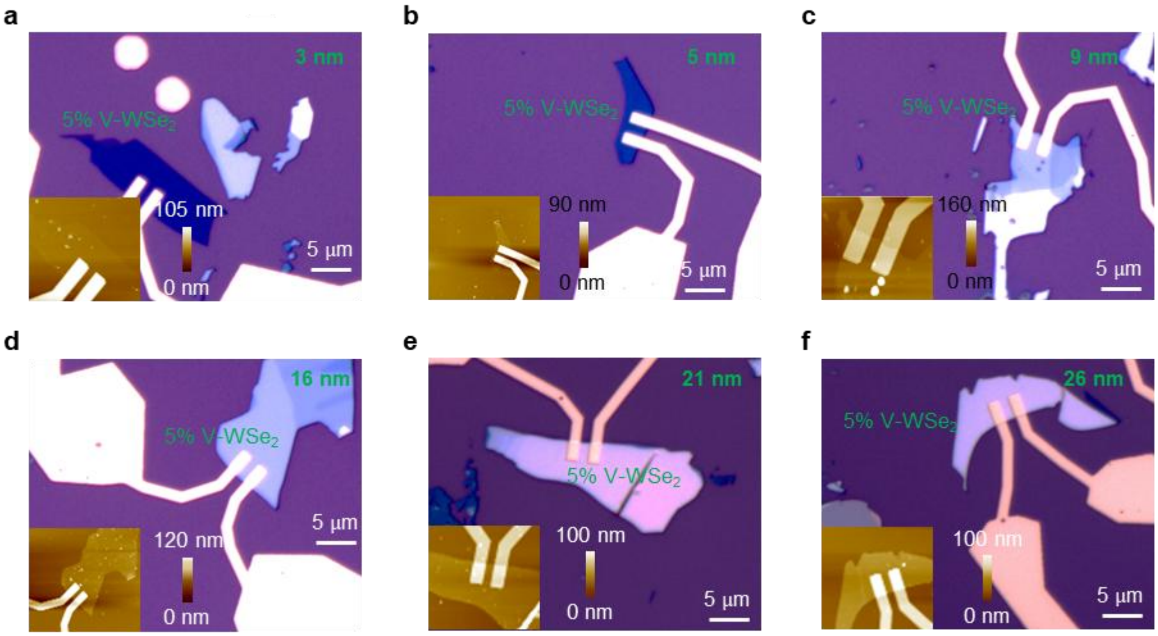

Supplementary Figure 8. Thickness characterization of 5% V-doped WSe_2 FET devices. (a–f) Optical microscopy images and AFM height profiles of 5% V-doped WSe_2 flakes with thicknesses of approximately 3, 5, 9, 16, 21, and 26 nm.

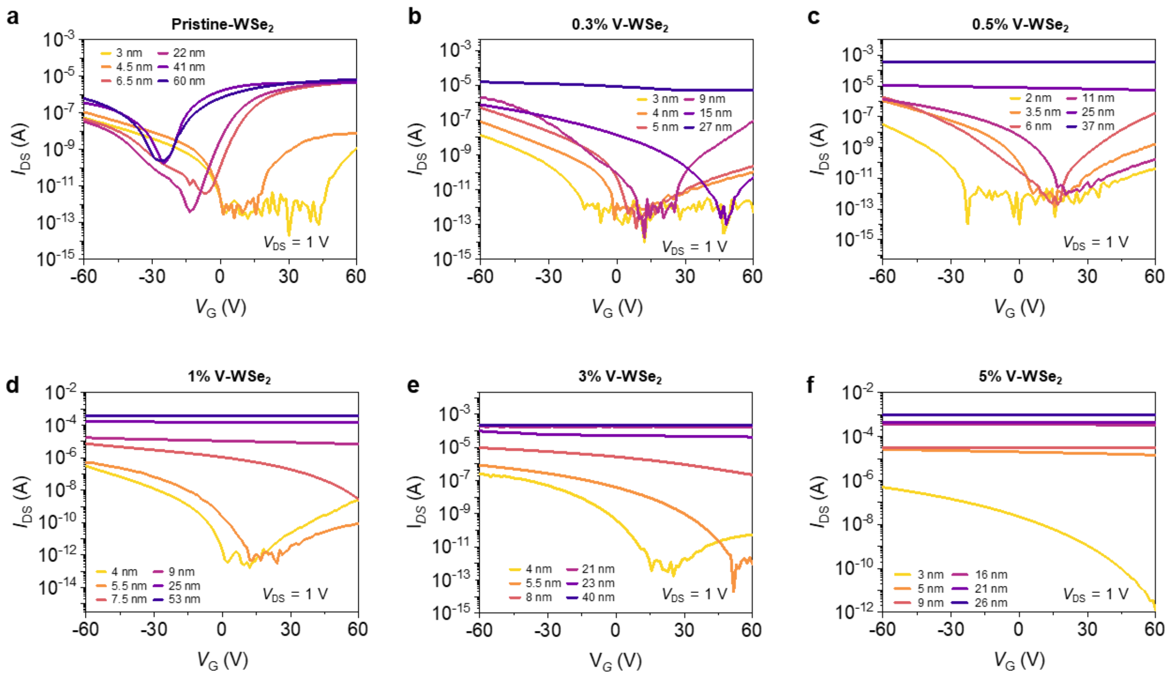

Supplementary Figure 9. Thickness-dependent transfer characteristics of pristine and V-doped WSe_2 (V_{DS} = 1 V). (a) Pristine WSe_2 devices exhibit a transition from p-type-dominant to n-type-dominant transport with increasing thickness. **(b–f)** V-doped WSe_2 (0.3–5%) shows suppressed ambipolarity and progressively enhanced p-type conduction with increasing dopant concentration, which is further strengthened in thicker layers, indicating thickness-tolerant p-type modulation. The transfer characteristics measured at a lower drain bias (V_{DS} = 1 V) confirm consistent behavior with those obtained at higher bias (V_{DS} = 3 V).

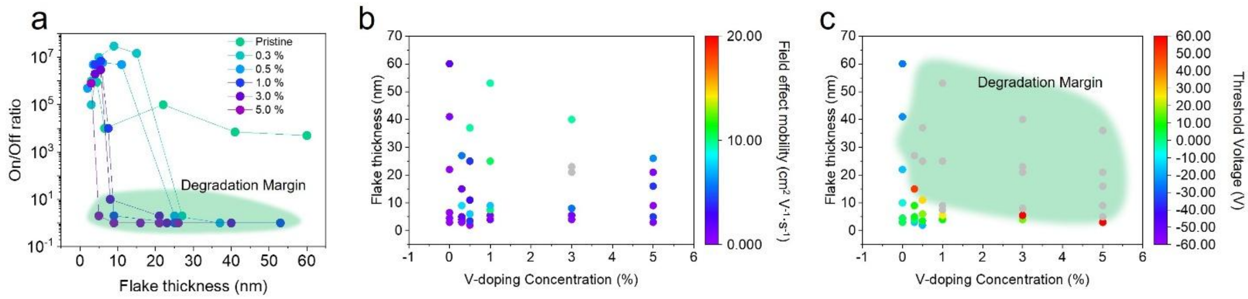

Supplementary Figure 10. **(a)** On/off current ratio as a function of flake thickness for pristine and V-doped WSe_2 devices with varying vanadium concentrations. Moderate doping (0.3–0.5%) enhances switching performance, while higher doping (≥3%) leads to degraded gate modulation and reduced on/off ratios, approaching degenerate behavior. The shaded region indicates the degradation regime. **(b)** Field-effect mobility (μ_{FE}) mapped as a function of flake thickness and V-doping concentration. Moderate doping (0.5–1%) yields enhanced and thickness-tolerant mobility (~8–10 cm^2 V^{-1} s^{-1}), whereas higher doping levels introduce increased variability due to impurity scattering and non-uniform dopant distribution. **(c)** Threshold voltage (V_{th}) extracted using a constant-current method (I_D= 1 nA), as a function of thickness and doping concentration. A systematic positive shift in V_{th} with increasing V concentration confirms effective p-type doping, while highly doped devices exhibit reduced gate tunability and less well-defined threshold behavior.

We systematically extracted key electrical parameters, including field-effect mobility (μ_{FE}), threshold voltage (V_{th}, defined at $I_D = 1\text{nA}$), and on/off current ratio for all devices shown in Fig. 2. The mobility was calculated using $\mu_{FE} = (L/WC_{ox}V_{DS})(dI_D/dV_G)$, where $L = 1\,\mu m$, $W = 2\,\mu m$, and C_{ox}corresponds to 300 nm SiO_2. As summarized in Fig. SXX, the results reveal a clear thickness- and doping-dependent transport behavior. Pristine WSe_2 exhibits relatively low mobility (<2 cm^2 V^{-1} s^{-1}) and strong thickness dependence, while moderate V doping (0.3–0.5%) enhances switching performance, yielding high on/off ratios (~10^7–10^8). Further increasing the doping concentration improves mobility, reaching ~8–10 cm^2 V^{-1} s^{-1} for 0.5–1% doping with minimal thickness dependence, indicating effective and uniform substitutional doping. However, higher doping levels (≥3%) lead to reduced on/off ratios and poorly defined threshold voltages due to increased off-state leakage and degenerate transport behavior. The threshold voltage systematically shifts toward more positive values with increasing V concentration, confirming p-type doping. Overall, these results identify an optimal doping window (~0.5–1%) that balances high mobility, strong gate modulation, and stable threshold behavior. The consistent trends across multiple devices further confirm the high crystalline quality and reliable dopant incorporation in V-doped WSe_2, while extracted values represent apparent mobility and exclude outliers arising from non-linear transport regimes.

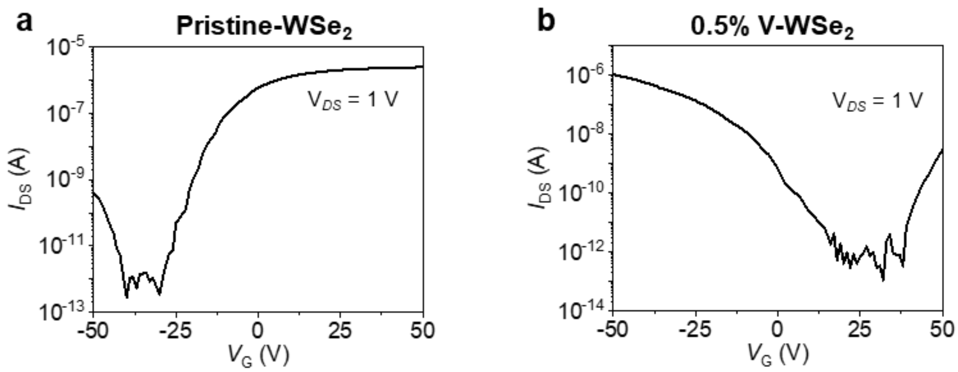

Supplementary Figure 11. Transfer characteristics of **(a)** pristine and **(b)** 0.5% V-doped WSe_2, respectively. The pristine WSe_2 exhibits n-type transport behavior, whereas the V-doped WSe_2 shows p-type transport behavior.

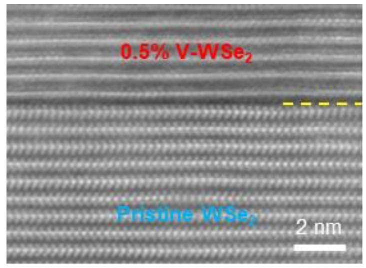

Supplementary Figure 12. Cross-sectional STEM image of a flexible V-doped/pristine WSe_2. The image reveals a well-defined van der Waals interface between the 0.5% V-doped WSe_2 (top) and pristine WSe_2 (bottom), with the vdWs interface preserved in the flexible device configuration. A slight relative rotational misalignment between the 0.5% V-doped WSe_2 and the pristine WSe_2 layers due to mechanically assembled vdWs heterostructures. The interlayer spacing between the 2 interfaces is consistent with the expected van der Waals gap in WSe_2 multilayers.

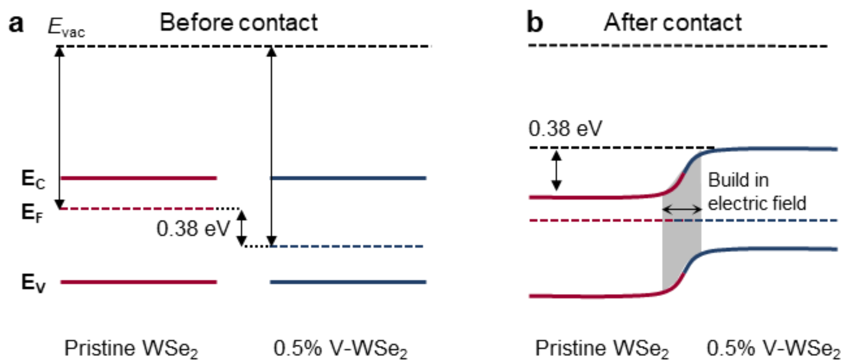

Supplementary Figure 13. Schematic energy band diagrams of pristine WSe_2 and 0.5% V-WSe_2 derived from KPFM measurement. (a) before contact, showing the work-function difference between pristine and doped WSe_2; **(b)** after contact, showing Fermi-level alignment, interfacial band bending, and formation of the built-in electric field.

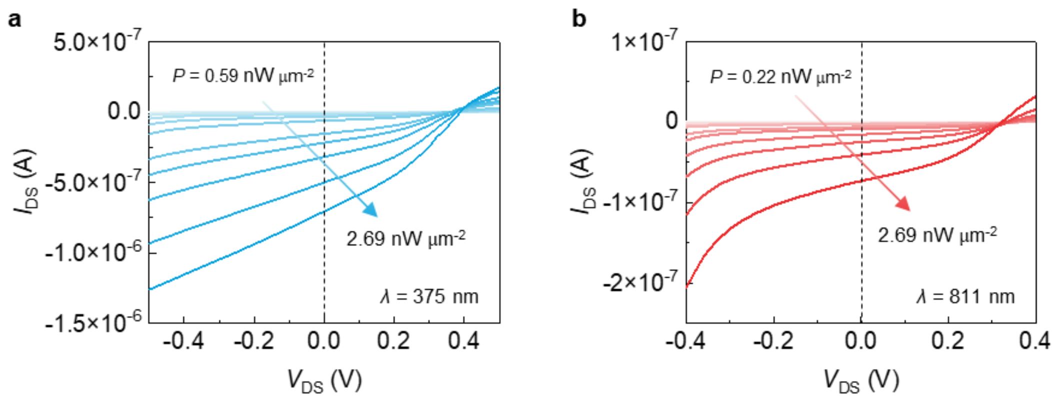

Supplementary Figure 14. Power-dependent photovoltaic response under different wavelengths (λ = 375 nm and 811 nm). Output characteristics of the 0.5% V-doped/pristine WSe_2 device measured under **(a)** 375 nm and **(b)** 811 nm laser illumination at varying incident power densities, demonstrating broadband photovoltaic operation

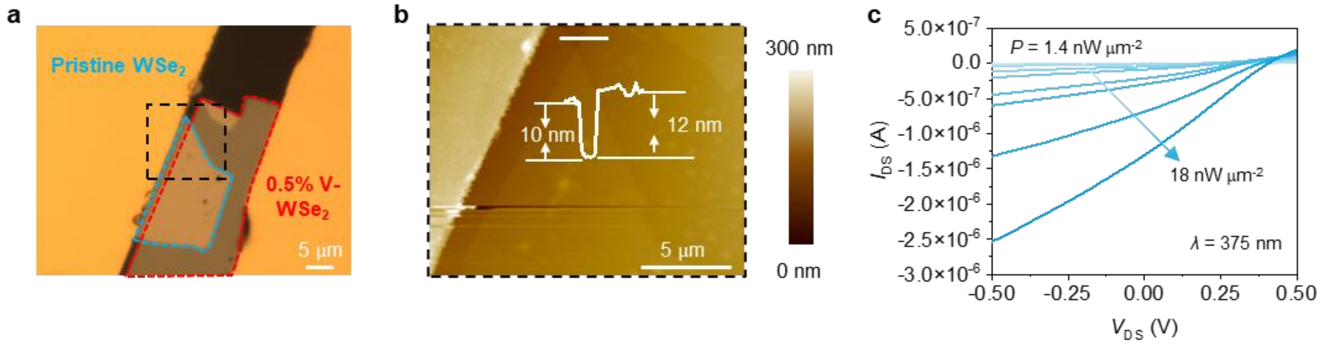

Supplementary Figure 15. Reproducibility of flexible V-doped/pristine WSe_2 homojunction devices. (**a**) Optical images of a representative flexible pristine/ 0.5% V-doped WSe_2 homojunction device. (**b**) Corresponding AFM topography, with inset height profiles, confirms thicknesses of approximately 12 nm for the 0.5% V-doped WSe_2 layer and 10 nm for the pristine WSe_2 layer. (**c**) Output characteristics measured under illumination at different incident optical powers, demonstrating a clear power-dependent photocurrent response. The repeated devices exhibit electrical and photoresponse characteristics comparable to those presented in the main text, confirming the reproducibility and reliability of the device performance.

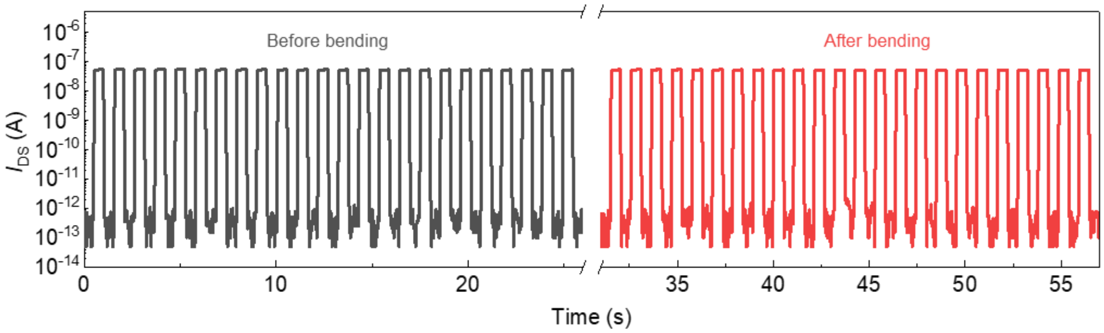

Supplementary Figure 16. Time-dependent photocurrent of the device at V_{DS} = 0 V before and after bending. The time-resolved I_{DS} under periodic light on/off cycles shows consistent photocurrent magnitude before and after bending, demonstrating the mechanical stability and reliable photoresponse of the device under deformation.

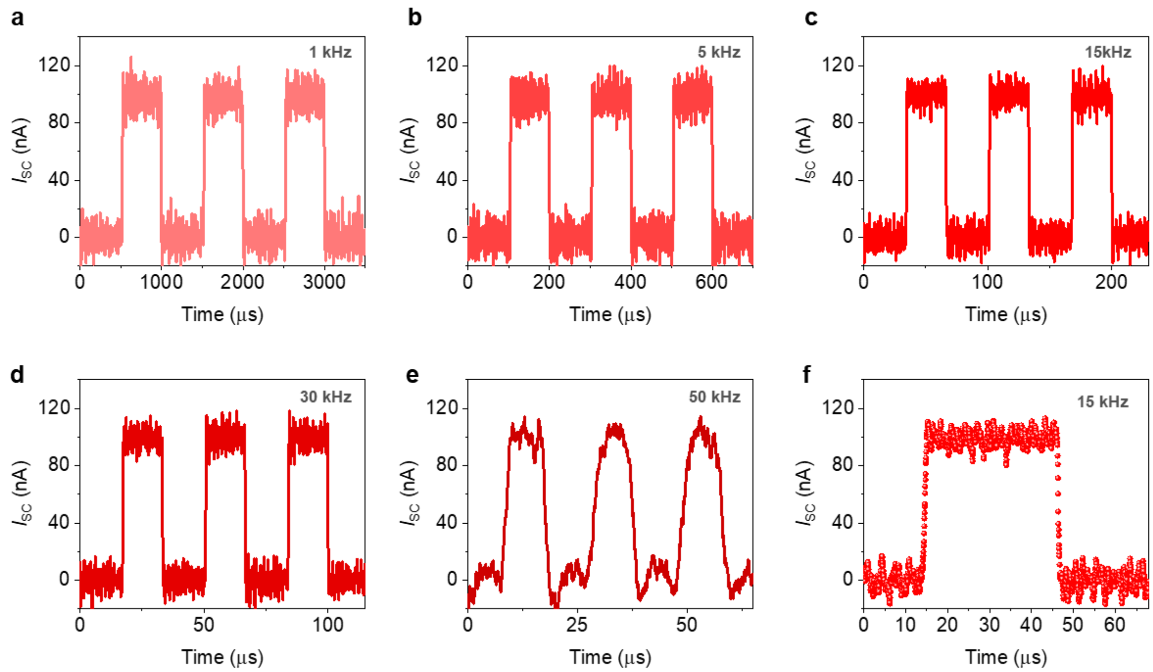

Supplementary Figure 17. Frequency-dependent photocurrent response of the device. (a–e) Time-resolved photocurrent measured under modulated illumination with frequencies ranging from 1 to 50 kHz, showing stable and nearly constant photocurrent amplitudes of ~ 100 nA across the entire frequency range. **(f)** Extracted photocurrent at 15 kHz, normalized to evaluate the fast response characteristics.

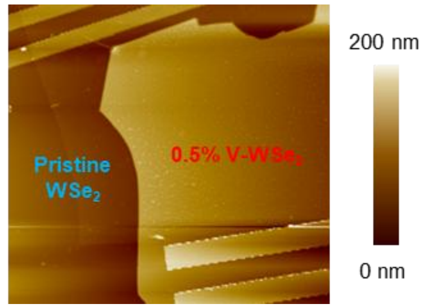

Supplementary Figure 18. AFM characterization of a thick V-doped/pristine WSe_2 heterostructure. AFM topography image showing thicknesses of approximately 52 nm for the 0.5% V-doped WSe_2 layer and 4 nm for the pristine WSe_2 layer.

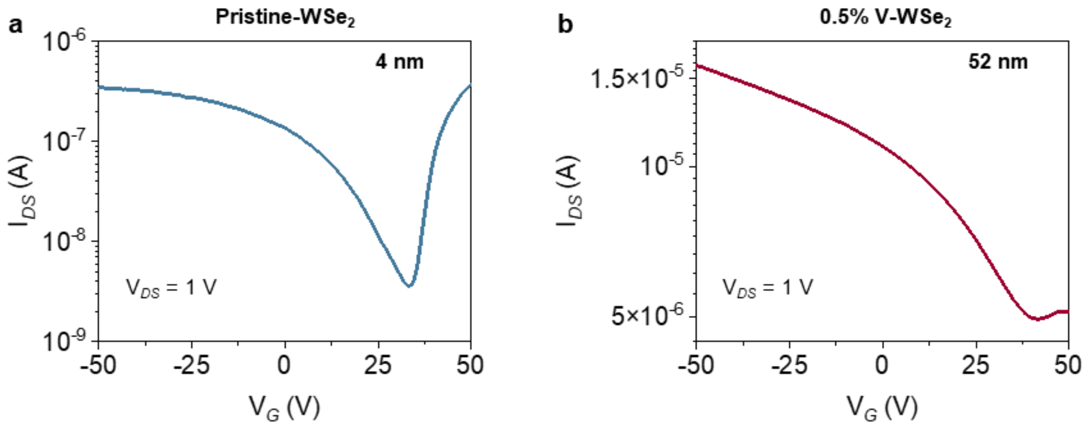

Supplementary Figure 19. Thickness-dependent gate modulation in pristine and V-doped WSe_2. (**a**) Transfer characteristics of a thin (~4 nm) pristine WSe_2 device, exhibiting strong gate modulation and ambipolar transport. **(b)** Transfer characteristics of a thick (~52 nm) 0.5% V-doped WSe_2 device, showing hole-dominated transport with weak gate dependence, indicative of degenerate p-type behavior.

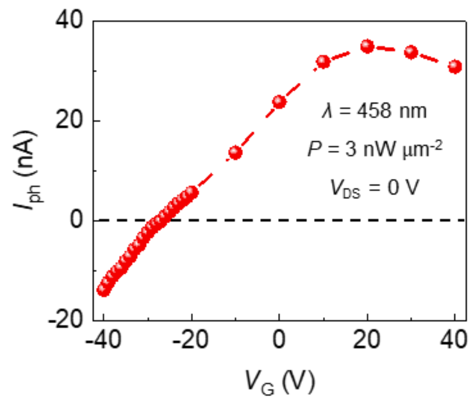

Supplementary Figure 20. **Gate-controlled photocurrent polarity switching.** Gate-dependent photocurrent measured at V_{DS} = 0 V under 458 nm illumination. The photocurrent reverses sign near $V_G \approx -27$ V, marking the transition between negative and positive photocurrent states and enabling encoding of signed photoresponsivity for in-sensor image-processing simulations.[1-2]

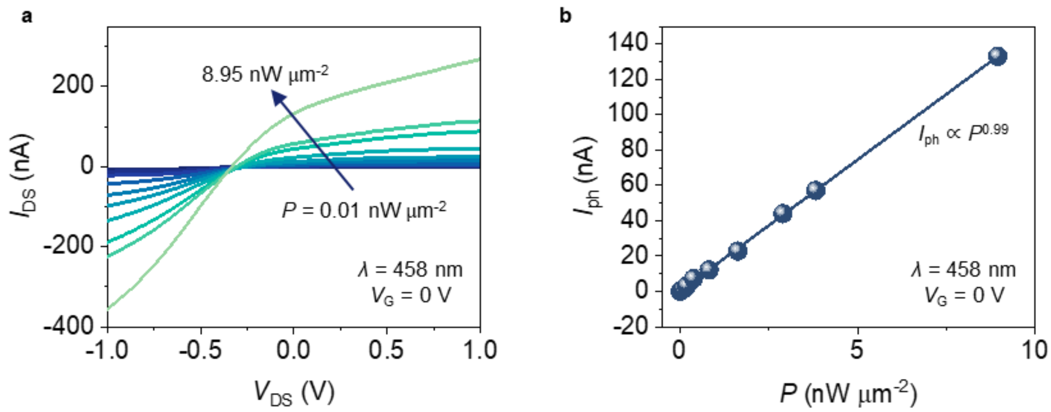

Supplementary Figure 21. Power-dependent photoresponse under 458 nm illumination. (a) Output characteristics measured at $V_G = 0$ V under increasing incident optical power densities. (b) Extracted photocurrent as a function of incident power, showing a near-linear dependence ($I_{ph} \propto P^{0.99}$), consistent with photovoltaic operation.

References

[1] L. Mennel, J. Symonowicz, S. Wachter, D. K. Polyushkin, A. J. Molina-Mendoza, T. Mueller, *Nature* **2020**, 579, 62.

[2] V. K. Dat, M. C. Nguyen, B. J. Jeong, N. T. Duong, V. D. Do, C. Hong, D. H. Phuong, V. T. Vu, J. Kang, X. Zhang, R. A. Taylor, K. Kyhm, W. J. Yu, J. Y. Choi, J. H. Kim, *Adv. Mater.* **2025**, 37, e00011.